ENVIRONMENTAL STUDIES

Vertical land motion in Greater New Orleans: Insights into underlying drivers and impact to flood protection infrastructure

Simone Fiaschi[1,2]*, Mead A. Allison[2], Cathleen E. Jones[3]

Vertical land motion is one of the main factors contributing to increased flood risk in coastal communities. Here, we use satellite interferometric synthetic aperture radar (InSAR) data to detect and measure previously undocumented land motions in Greater New Orleans (GNO), Louisiana. Although most of New Orleans is generally stable, rapid elevation loss occurs in parts of the city (up to −20 millimeters per year) and on flood protection walls constructed following Hurricane Katrina (up to −28 millimeters per year). This work provides unprecedented spatial coverage of land motion rates in GNO, including wetlands and the flood protection system previously lacking data, which allows a more detailed examination of ground deformation patterns and insight into underlying drivers. In the broader context, this work shows the potential of InSAR for measuring localized land motion in New Orleans and similar communities, particularly where the presence of wetlands complicates its application.

INTRODUCTION

As with a substantial number of other coastal cities around the globe (*1*), the City of New Orleans in the Mississippi Delta (MD) in southern Louisiana, USA (Fig. 1) is at risk of catastrophic flooding, both from the Mississippi River and from ocean flooding, as was observed in Hurricane Katrina in 2005 (*2*). The vulnerability of New Orleans and other similar global population centers is due to its presence in the low-elevation coastal zone (<10 m) and to subsurface geologic controls. Accelerating sea level rise exposes coastal-river cities to increased flood risk due to storm surges. This risk is magnified in coastal cities by the presence of vertical motion of land that is caused by a multitude of natural and anthropogenic factors (*3*, *4*). The most important natural factor is land subsidence, a settling of the Earth's surface chiefly driven by sediment compaction in the deltaic-coastal geomorphic setting of New Orleans (*5*). However, anthropogenic factors, such as groundwater pumping for increased drinking water supply, oil and gas withdrawals, or land-use changes, are contributing causes to the exacerbated sea level rise rates occurring in densely populated coastal areas (*4*). Groundwater extraction is practiced in Greater New Orleans (GNO) for a variety of purposes (*6*, *7*), which has left portions of the metropolitan area at or below sea level. Vertical land motion (defined by negative rates for elevation loss and by positive rates for elevation gain) in low-elevation coastal regions not only compounds urban resilience in the face of relative (absolute plus vertical land motion) sea level rise but also degrades drainage and sewage systems and rainfall runoff, which contributes to nuisance flooding that causes damage to property and infrastructure (*8*). The river-side location of New Orleans also presents a preferential pathway of storm surges moving inland from the ocean (*9*). Relative sea level rise progressively degrades the level of storm surge protection offered by the Hurricane and Storm Damage Risk Reduction System (HSDRRS) of floodwalls and levees, gated structures, and pump stations surrounding GNO that was constructed after Hurricane Katrina at a cost of approximately US $15 billion (see www.mvn.usace.army.mil/Missions/HSDRRS/). This progressive increase in risk is particularly acute because of recent observed acceleration in the rate of Gulf of Mexico sea level rise (*10*). Reductions in ground elevation relative to sea level due to historic and recent subsidence likely not only played a part in levee failure in Hurricane Katrina but also accounted for the extreme post-storm flooding depths (>2.5 m) in parts of the city (*11*). Understanding ongoing factors such as subsidence and fluid withdrawal that affect elevation of river-coastal cities is a key prerequisite to developing viable and long-term sustainability measures and resilient design criteria.

Interferometric synthetic aperture radar (InSAR) is a remote sensing technique for mapping changes in the shape or position of the ground surface, also referred to as ground deformation, using microwave radar images of the Earth's surface (*12*) obtained from airborne, ground-based or satellite systems. Because of its high temporal (days to weeks) and spatial (~0.5 to 50 m) resolution, and large area coverage (~25- to 35^3-km^2 image footprint), satellite-based InSAR is a valuable tool for tracking and measuring subsidence in urban areas and in deltas around the world, both to quantify the rising threat for low elevation coastal areas and to examine natural and anthropogenic drivers (*13*, *14*). The objectives of the present study are as follows: (i) to use InSAR time-series analysis to obtain additional constraints on negative vertical land motion rates in the GNO metropolitan area and to identify possible drivers; this objective builds upon two earlier InSAR studies of GNO (*15*, *16*) that we describe in detail below; (ii) to examine the applicability of freely available InSAR data collected by the Sentinel-1A (S1A) satellite to examine natural wetland areas surrounding urbanized GNO and in the MD at large; and (iii) to examine potential rates and causality of HSDRRS elevation loss as part of an effort to recertify the system's level of storm surge protection (*17*).

Background

Since Hurricane Katrina, acquisition and study of various types of geological data and ground-borne, air-borne, and space-borne geodetic data have provided valuable insights into the rates and patterns

[1]TRE-ALTAMIRA Inc., Vancouver, BC, Canada. [2]Department of River-Coastal Science and Engineering, Tulane University, New Orleans, LA, USA. [3]Jet Propulsion Laboratory, California Institute of Technology, Pasadena, CA, USA.
*Corresponding author. Email: simone.fiaschi@tre-altamira.com

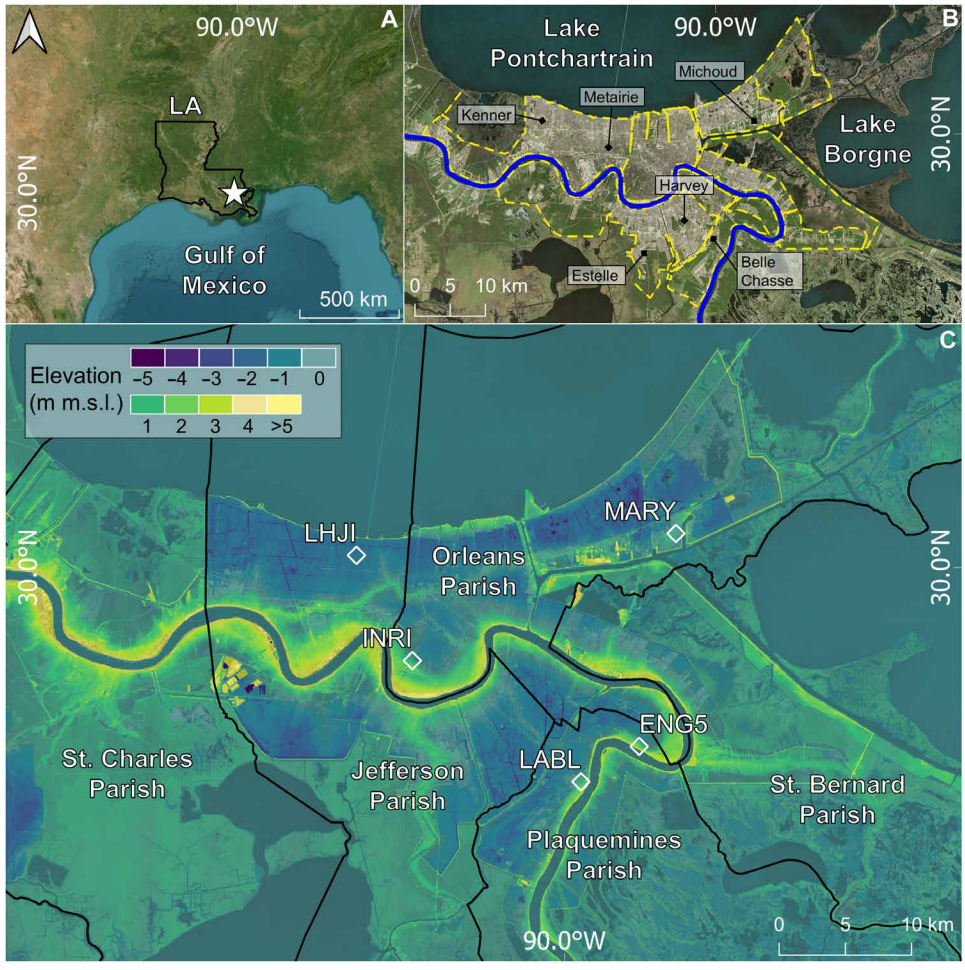

Fig. 1. Overview of the study area. (**A**) Location of the state of Louisiana (LA), USA, and the city of New Orleans (white star); base map is derived from ESRI Satellite World Imagery. (**B**) Satellite optical image of GNO; the blue line is the course of the Mississippi River; the yellow dashed line is the extent of the HSDRRS; base map is derived from Bing Maps Satellite Imagery. (**C**) Elevation map of GNO in m above mean sea level (m.s.l.), based on the 2023 US Geological Survey (USGS) $^{1}/_{3}$–arc-sec digital elevation model (DEM), WGS84 coordinate system; the black lines mark the Parishes subdivisions of the metropolitan area; the white polygons and four-letter station code names are the location of the available continuous Global Positioning System (GPS) stations.

of vertical land motion in the MD and in GNO, defined here as the city and surrounding urban portions of Jefferson, St. Bernard, and Plaquemines parishes encompassed by the HSDRRS (Fig. 1). However, the markedly different vertical motion rate estimates in the various studies have been hard to reconcile and can seldom be unequivocally linked to underlying causative processes [e.g., natural and anthropogenic drivers; (*18*)]. Relative sea level change reconstructions using age-dating of Holocene basal peat overlying the Pleistocene strata in several parts of the MD indicate that Pleistocene and deeper units have been virtually stable over most of the Holocene (*19*), showing subsidence less than −1 mm/year over timescales of millennia. Dokka *et al.* (*20*, *21*), in contrast, reported subsidence rates up to tens of millimeters per year from the 1970s to 1995 for several benchmarks on long pile foundations extending into Pleistocene and deeper strata in the surroundings of Michoud in GNO (location in Fig. 1B). They proposed a role for (neo)tectonic activity associated with the Michoud fault or industrial groundwater extraction in that area (locations in Fig. 2A). Global Positioning System (GPS) station ENG1/ENG5 (locations in Fig. 1), some 15 km south of Michoud, showed much less vertical motion of about −2 mm/year since the 1990s (*22*). For a more recent period (2014–2020), Karegar *et al.* (*23*) used a combination of conventional GPS and GPS Interferometric Reflectometry (GPS-IR) to estimate uplift of +2.2 ± 0.7 mm/year occurring at a depth > 2000 m at GPS station MARY at the NASA Michoud facility, while subsurface layers shallower than 2000 m contribute −2.5 ± 1.3 mm/year of motion. They suggested that the deep uplift is due to cessation of nearby groundwater withdrawal for industrial cooling in 2016. The logic of this interpretation is unclear, however, because groundwater pumping occurs at depths of a few hundreds of meters. South of GNO and toward the birdfoot of the MD, other studies (*24*–*26*) inferred subsidence rates between −5 and −10 mm/year during the late 20th century from geodetic leveling data and tide gauge records and linked to the impacts of hydrocarbon production, further suggesting that the upper Pleistocene section may not be stable at present. At the same time, however, this remains a matter of interpretation as the depth to the Pleistocene interface increases rapidly toward the SE and a considerable thickness of Holocene strata occurs even below deeply

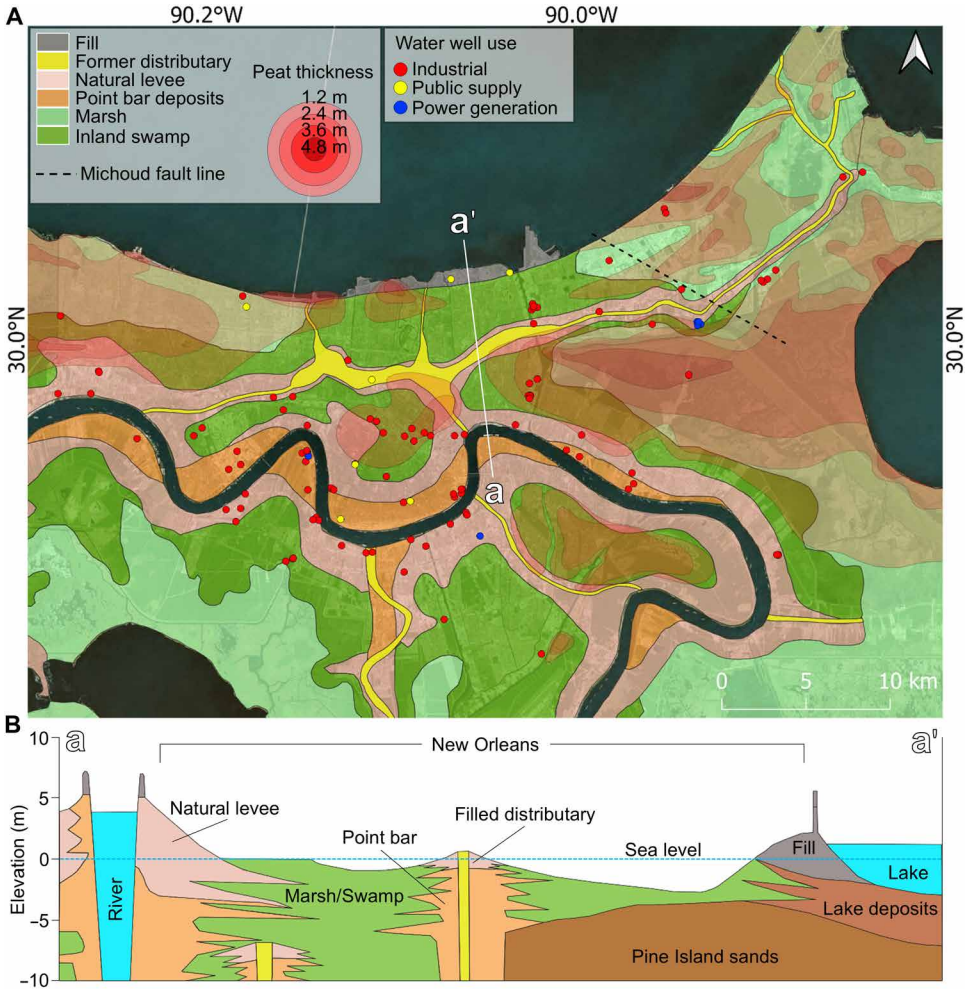

Fig. 2. Geological map of the study area. (**A**) Schematic distribution of the Holocene deposits in GNO (*59*, *60*); the transparent red areas show the distribution and thickness of the surficial peat deposits (*61*); the dashed black line is the approximate location of the Michoud fault (*21*); the colored points are the active water wells as of May 2025 (data available from the Louisiana Department of Natural Resources, www.sonris.com/); base map is derived from Bing Maps Satellite Imagery. (**B**) Vertical cross section of the Holocene deposits along the a-a′ white line shown in part (A) [from (*59*)].

founded benchmarks, which implies that it cannot be ruled out that most of this subsidence originates from compaction of the Holocene interval of soft sediments (*27*).

Several studies have shown that subsidence rates in the MD generally correlate with the thickness of Holocene sediments (Fig. 2) (*22*, *28*–*31*). Using rod surface-elevation table (RSET)–marker horizon stations, Jankowski *et al.* (*31*) inferred compaction-driven subsidence within the top ~20 m of Holocene strata to be between −5 and −15 mm/year over periods of 8 to 10 years. This demonstrates the potentially large contribution of natural compaction to surficial land subsidence and land loss in the MD. More recent geotechnical modeling has suggested that the vast majority of this compactional subsidence is associated with the near-surface (1 to 3 m thick) compaction of recent organic-rich wetland layers (Fig. 2) (*32*). Only limited areas of remnant wetland are present today within the HSDRRS, and, in the urban setting of MD beneath GNO, land subsidence tends to be compounded by loading and drainage-induced compaction and mass-loss associated with oxidation of organic-rich soils (*33*). Neighborhoods bordering Lake Pontchartrain (Fig. 1) that were formerly cypress swamps and freshwater marshes have subsided up to 3 m in about two centuries at rates up to −30 mm/year (*8*). At present, these rates are more subdued but, nevertheless, represent an ongoing potential source of subsidence where compaction- and oxidation-sensitive strata (*7*) remain in locations where the groundwater table has been deflated by extraction (*8*).

Satellite-based InSAR provides the most comprehensive information about land surface deformation in GNO due to the aforementioned unprecedented spatial coverage and potentially high temporal resolution. To date, only few InSAR studies (*15*, *16*, *34*–*36*) have been conducted over GNO. Dixon *et al.* (*15*) used 33 C-band RADARSAT-1 (RSAT) SAR images to derive linear deformation rate estimates covering 2002–2005 processed using the permanent scatterer interferometry (PSI) technique (*37*). Their map revealed spatial patterns of vertical land motion in the urban area between Lake Pontchartrain and the Mississippi River: Rates varied from low elevation loss values between 0 and −2 mm/year in downtown New Orleans to relatively high values between −8 and −13 mm/year in Lakeshore and at the eastern half of the East New Orleans district and at Michoud (fig. S1A). Although their results represent an unprecedented view of the movements affecting the GNO, high uncertainty

levels of the obtained rates (mean and SD of rate for all the points was −5.6 ± 2.5 mm/year) make it difficult to interpret the results at the local scale.

Jones *et al.* (*16*) derived a deformation velocity map from two L-band SAR images obtained with NASA's Uninhabited Aerial Vehicle SAR (UAVSAR) covering the period from June 2009 to July 2012. Their results showed markedly different deformation patterns from the earlier study, including uplift in the New Orleans East district, very high vertical motion rates of <−30 mm/year at Michoud, and rather high rates between −10 and −20 mm/year along the banks of the Mississippi River (fig. S1B). However, the uncertainty of these results is generally high as the ratio of measured rate to the estimated uncertainty is close to or exceeds one. Their data did, nonetheless, convincingly reveal local impacts of industrial groundwater pumping (Norco refinery) and of recent housing development construction (Westwego, Louisiana) that likely reflects surface loading. These impacts are better resolved in the airborne data because uncertainty of differential movement over relatively short distances in areas of stronger deformation rates is relatively small.

Qu *et al.* (*34*) monitored vertical ground motion over the Gulf coast of the USA, including GNO, using ALOS-1 PALSAR L-band SAR imagery between 2007 and 2011. Their results show average vertical motion rates over the populated areas of GNO between −5 and −25 mm/year, and maximum rates of −52 mm/year recorded at sections of the canal located East of the city. According to the authors, the measured rates are generally in good agreement with the previous works of both (*15*) and (*16*), while the only discrepancy reported is the absence of subsidence detected in the Norco area measured, instead, by Jones *et al.* (*16*) between 2009 and 2012. They detected localized subsidence at the south shore of lake Pontchartrain and at several communities such as Kenner, Michoud, and Metairie. They found higher subsidence signals in both urban and industrial areas of Estelle, Harvey, and Belle Chasse (locations in Fig. 1B), as well as areas of minor uplift of unknown origin south of Kenner and in the central part of Michoud. These results, nonetheless, present some limitations due to the absence of data coverage in critical areas of GNO such as the wetlands surrounding the city and to the adopted L-band dataset, which is not sensitive to rates up to a few millimeters per year. These make it impossible to distinguish between real signal and noise in areas of subtle ground motion.

More recent large-scale InSAR studies provided maps of rate of motion of the contiguous USA coastline (*35*) and the Gulf coast (*36*) that have comparative value for GNO. Using a combination of ALOS-1 PALSAR and S1A images acquired between 2007 and 2020, Ohenhen *et al.* (*35*) show that only minor subsidence is affecting GNO, with rates ranging from −1 to −2 mm/year, which is within the uncertainty levels of the proposed approach. On the other hand, Wang *et al.* (*36*) analyzed 103 S1A images from 2017 to 2020 and obtained vertical land motion that is mainly positive over the city of New Orleans, showing rates between +2 and +4 mm/year Their map depicts also three main areas of elevation loss located at the international airport (rates up to −17 mm/year), at Harvey (rates up to −21 mm/year), and in vegetated areas East of the city (rates up to −34 mm/year). Due to limited computational capabilities, time availability, and resources, the results obtained through large-sale InSAR approaches, which often rely on semi or fully automated processing chains, generally lack the level of precision and detail required to fully capture the surface dynamics occurring at much smaller scale. For this reason, such studies, even if their scientific contribution to support coastal resilience at the regional scale is unquestionable, have been unable to resolve total ground motion and its underlying mechanisms to the degree necessary for future sustainability planning for coastal urban areas such as GNO. Furthermore, ascertaining to what extent the differences between these four studies reflect true differences in deformation rates is not trivial because of differences in datasets (radar band used, acquisition method, and number of images), time intervals, and processing methods adopted that yield large variations in data coverage, ground resolution, and uncertainties in rates.

This study introduces two key advancements in InSAR analysis over GNO. First, it leverages a S1A dataset from 2016 to 2020, providing unprecedented spatial coverage of ground deformation across both urban and natural environments, including areas previously lacking data, such as wetlands, which allowed for a more detailed examination of ground motion patterns. Furthermore, the S1A data permitted an analysis of motion rates along the HSDRRS, for which, to our knowledge, comprehensive elevation monitoring surveys are not routinely conducted. Second, we reprocessed RSAT data previously analyzed by Dixon *et al.* (*15*) and extended to 2007 using an advanced technique, enabling a more detailed and accurate assessment of ground motion over a longer time period than possible with the S1A data alone.

RESULTS

Results for GNO in 2002–2007 (RSAT)

The average vertical velocity map (Fig. 3A) illustrates the current RSAT InSAR results over GNO. For each point, representing a pixel of around 15 m by 6 m, negative values mean movement farther from the satellite (potentially representing loss of surface elevation), the positive values mean movement toward the satellite (potentially representing increase of surface elevation). The points with velocities in the range of ±2 mm/year (in green) are the ones considered as "stable" (e.g., movement within the error range). In addition to the average velocity rate from beginning (2002) to end (2007) of the image record, each measured point has a displacement value associated with it in each of the 52 image dates, which provide the accumulated displacement in time starting from the first date.

In total, we obtained 791,377 measured points, with an average vertical velocity of −1.3 ± 0.9 mm/year and a density of ~591 points/km^2. The point distribution is mainly controlled by the temporal coherence of the targets at the surface, an indicator (from 0 to 1) of the level of noise in the phase domain of the InSAR pixels. We obtained most of the points over the urbanized area of the GNO, where linear infrastructure such as bridges, roads, and the pre–Katrina flood control system appears as valid InSAR targets. While most of the vegetated areas outside the city limits do not provide measure points because they have coherence below the used coherence threshold of 0.60, some portions of the wetlands located in the eastern side of the city fell above this cutoff (Fig. 3). Averaging the full measured point population, GNO is stable in the 2002–2007 period, with 66% of points showing motion in the range of ±2 mm/year. We found areas of higher elevation loss from −4 to −8 mm/year (in yellow, Fig. 3) in Jefferson Parish in the residential areas of Kenner, north of the Louis Armstrong International Airport, and in the vicinity of Harvey in the south. Similar rates are also present in the Michoud area in the northeast of the study area. Localized areas of greater elevation loss (<−15 mm/year) are present at the Louis

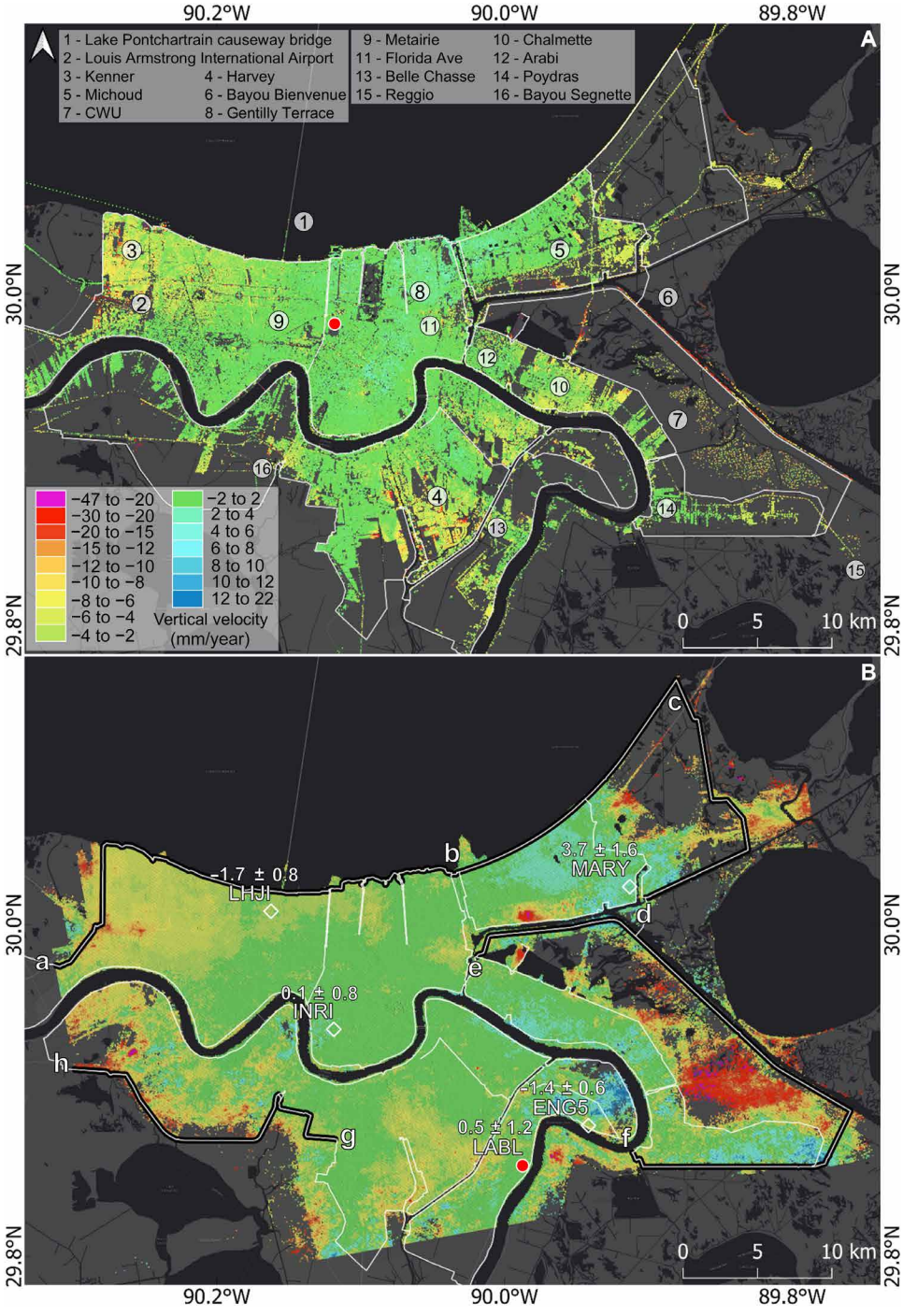

Fig. 3. InSAR-derived average relative vertical velocity maps. (**A**) The 2002–2007 RSAT results. (**B**) The 2016–2020 S1A results. The red circles are the location of the reference point used for the InSAR processing. The white lines in (A) are the HSDRRS floodwalls and levees enclosing the city and surrounding areas of Jefferson and St. Bernard Parish constructed after 2007. In (B), the black and white lines marked with letters from "a" to "h" are the profiles used to extract the velocity rates along the flood protection system and presented in Fig. 8. In (B), the labeled white squares are the locations of the available continuous GPS stations, reported with the corresponding average vertical velocity rates (in millimeters per year). The underlying base map is provided by Esri, HERE, OpenStreetMap.

Armstrong International Airport, at some industrial and newly constructed residential buildings in Harvey, at a few industrial sites in Michoud, and along the small strip of land crossing the Bayou Bienvenue Central Wetland Unit (CWU). The flood walls east of the CWU presents maximum rates of elevation loss up to −47 mm/year Here, the rates are not uniform along the entire concrete floodwall but generally decrease moving away from the central portion of the wall in the area close to Lake Borgne. Localized areas with rates up to +6 mm/year are present in downtown New Orleans and in the Gentilly Terrace district.

Results for GNO in 2016–2020 (S1A)

Analysis of the S1A dataset provided a total of 163,204 points in the GNO image scene. Average velocity is −2.8 ± 0.7 mm/year and point density is ~134 points/km^2. Reflecting the different approach adopted and the lower coherence cutoff (see Materials and Methods for details), we obtained points over most of GNO, improving upon the 2002–2007 RSAT coverage, and including some vegetated areas (wetlands) inside and outside of the urban areas of the City of New Orleans. The few areas inside the HSDRRS without coverage are those (presumably) characterized by surficial water, both permanent (e.g., bayous and lakes) and temporary (e.g., tidally or seasonally flooded wetlands) that do not provide reliable InSAR phase information.

As a general overlook, the spatial distribution and rates of the motion resulting from the analysis of the S1A images are comparable to the ones obtained with the RSAT images. The S1A results show a larger areal extent of the locations with relatively rapid elevation loss (up to −10 mm/year). These rates are present not only in the cities of Kenner and Harvey but also in the lakefront north of Metairie (Fig. 3). Our results reveal higher localized elevation loss rates at the Louis Armstrong International Airport, at industrial sites south of the English Turn and in the Michoud area. Maximum rates of elevation loss, between −30 and −47 mm/year, are affecting a large portion of the imaged wetlands, particularly the CWU and the marshes in the northeast of the study area, outside the New Orleans city limits. Sections of the HSDRRS flood protection system around GNO are experiencing different rates of movement, as discussed below. The S1A results also show areas of elevation gain with rates up to +8 mm/year in Michoud near the MARY GPS station and in Chalmette in the St Bernard Parish. We found further areas showing elevation gain in vegetated areas north of the ENG5 GPS station and in the southeastern portion of the study area, in proximity to a flood wall, where the rates reach +23 mm/year

DISCUSSION

Importance of satellite and processing methodologies

As outlined in earlier sections, we used two SAR satellites (RSAT and S1A) to examine land elevation change in GNO in the period from 2002 to 2020. In theory, the resurvey of a fixed area provides an opportunity to examine the impact of sensor characteristics and processing methodology on the measured average velocities. However, several substantial natural and human changes marked the 18-year period of record in the GNO landscape. Hence, we must take into account the different time intervals over which the satellite processing occurred for this and previous studies (Table 1 and table S2) when comparing results. Key specific changes include (i) the storm surge and extensive and long-lasting (weeks to several months) flooding inside the GNO flood protection system by Hurricane Katrina in August 2005, (ii) construction of the new HSDRRS flood protection system in 2011–2017, (iii) changing point-source groundwater withdrawal, and (iv) ground elevation changes linked to construction and excavation projects in this highly urbanized area.

As previously noted, the uncertainties associated with the measured displacement rates obtained by both Dixon *et al.* (*15*) covering 2002–2007 using RSAT data and the PSI method and by Jones *et al.* (*16*) using the UAVSAR L-band system are too large to allow meaningful direct comparison with their rate estimates. For this reason, we considered it necessary to reprocess the RSAT data with a more recent processing algorithm to obtain results that are more comparable with the S1A data of this study. The RSAT and S1A results (Fig. 3) are mutually consistent in the central part of the study area where there is no evident ground motion (rates generally in the

Table 1. Characteristics of the InSAR datasets used in this study. NA, not available; rg, range; az, azimuth; HH, horizontal horizontal; VV, vertical vertical; PS, permanent scatterer; DS, distributed scatterer.

SAR system	RADARSAT-1	Sentinel-1A
Sensing period (dd/mm/yyyy)	14/04/2002 24/02/2007	28/01/2016 31/03/2020
Track number	294	165
Orbit	Ascending	Ascending
Revisit time (days)	24	12
Look angle (°)	29.0	39.6
Radar band/λ (cm)	C/5.6	C/5.6
Polarization	HH	VV
# of scenes	52	107
# of interferograms	1326	585
Max temporal baseline (days)	1777	168
Max perpendicular baseline (m)	NA	233
Ground resolution (m) (rg az)	14.7 × 5.4	2.3 × 14.1 (~60 × 60 with multilook)
Scatterer type	PS/DS	DS

range of ±2 mm/year), as displayed in the map of velocity difference between the two datasets (Fig. 4, in white). There is good agreement also in the low rates of vertical motion occurring in the Kenner and Harvey urban areas, as well as some of the industrial sites along the Mississippi River. In other areas of GNO there are notable differences. The areal extent of the 2016–2020 S1A-derived negative motion is larger than those of the 2002–2007 RSAT, although with similar rates. We interpret this as a result of the lower resolution approach adopted for the processing of the S1A data in respect to RSAT data, which produced better point coverage to the detriment of the sensitivity to detect small changes in the rates of motion occurring over short distances. This is visible east of the Kenner area (Fig. 3) where the measured surface motion, even if similar in rate, appears averaged over a larger extent in the S1A results. Greater differences in the detected rates between the two datasets occur in several areas of the urban GNO. The areas with the most change are at and south of the Louis Armstrong International Airport, at Michoud, and at Chalmette (Fig. 4, respectively, A, B, and C). While, in the first two areas, we mainly attribute these differences to real changes in the underlying factors controlling ground motion during the two monitored periods, the origin of the different motion in the latter area remains unclear. We can explain this by taking into account both technical and natural factors: The motion detected here is the results of the averaging of the phase contribution of both man-made structures and the adjacent marshlands that may dominate such signal. Anthropogenic factors in Chalmette, such as changes in operational activities of the industrial site on the banks of the Mississippi River or the construction of the flood protection system north of the area, may also add another degree of complexity to the detected motions during 2016–2020.

It is clear that the technical approach used to process InSAR data (i.e., processing algorithm and parameters) together with the choice of the satellite sensor (i.e., but not limited to, incidence angle, pixel resolution, temporal coverage, and radar wavelength) has a major impact on the type of information that can be extracted from any study area, and this is particularly true in complex environments such as river deltas. The choice of the reference point in an InSAR time-series analysis, when varied between studies, can introduce uncompensated biases in motion rates, adding complexity to comparisons. However, if we select the reference point correctly, assuming that the selected pixel does not present relevant motion or trends while showing robust and consistent phase reflectivity, then we can consider the impact of such selection on the obtained results negligible. The velocity difference of Fig. 4 shows that the locations selected for the reference point of RSAT and S1A is also stable in each of the other satellite's results, with differences below 0.5 mm/year for both areas.

The results of the current work and previous studies, despite their differences, all contribute in different ways to the understanding of the dynamics of the ground deformations in GNO and provide further insights into the capabilities of InSAR instruments for precisely detecting and monitoring these land motions.

Sources of ground motion in urban GNO

The S1A results shown in Fig. 3B and in the sites highlighted in Fig. 5 indicate that most of the urban area, and, in particular, its central part in the core of the City of New Orleans, is relatively stable (green in Fig. 5A). The stable area also includes developed portions of eastern Jefferson Parish on the east bank of the river, west bank Jefferson Parish in areas proximal to the river, and St. Bernard Parish near the river in the Chalmette-Arabi corridor (refer to Fig. 3A for locations). This pattern broadly agrees with the older InSAR studies (*15*, *16*, *33*) and even more consistently with the RSAT results of this study (Fig. 3A). Other urbanized areas, particularly in western Jefferson Parish (Kenner) on the east bank of the river, along the Lake Pontchartrain frontages in New Orleans (Fig. 5A), and distal

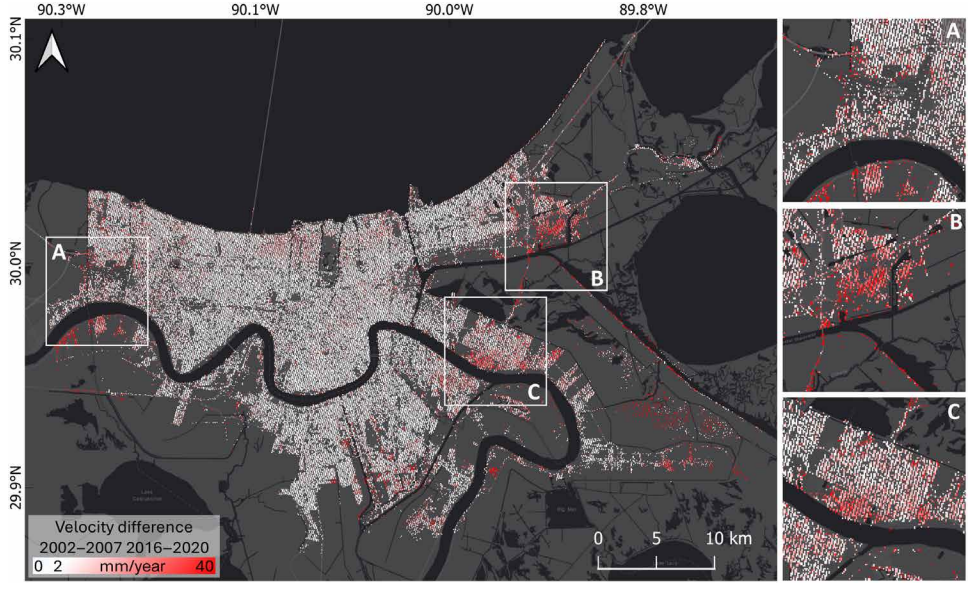

Fig. 4. Velocity difference between the RSAT (2002–2007) and S1A (2016–2020) InSAR results. The panels are the areas with high changes discussed in the text: (**A**) Luis Armstrong International Airport; (**B**) Michoud; (**C**) Chalmette. The values in the map are the modulus of the difference between the S1A and RSAT mean velocity rates after sampling the data to a common grid of 60 m (lowest resolution between the two datasets). Scale goes from 0 to 2 mm/year (in white, no substantial change) to 40 mm/year (in red, high change). The underlying base map is provided by Esri, HERE, OpenStreetMap.

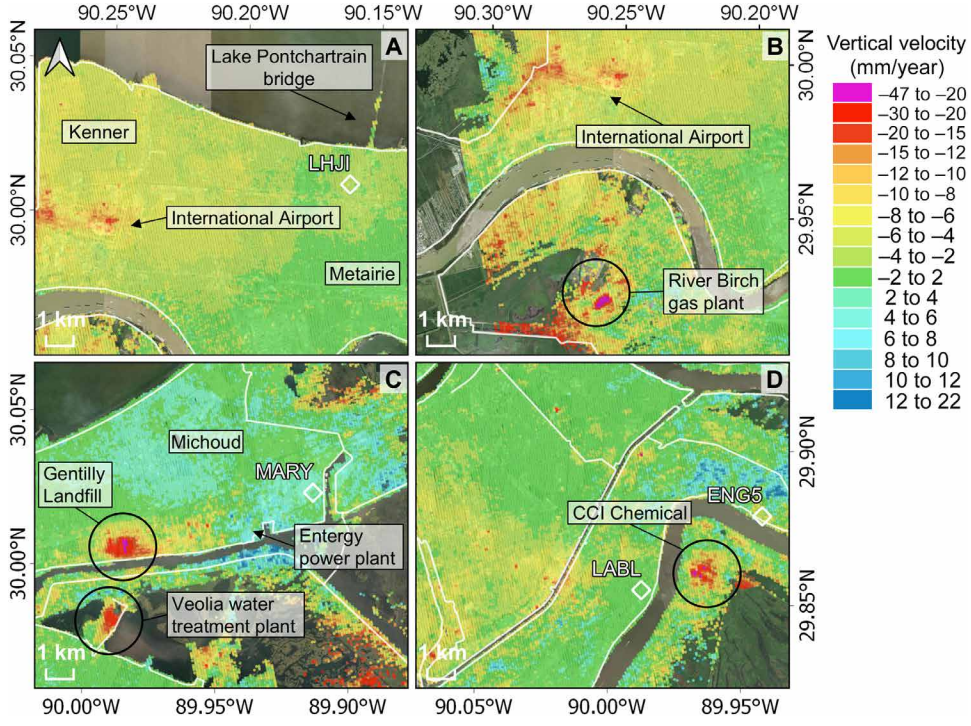

Fig. 5. Close-ups of the S1A results obtained over GNO. (**A**) New Orleans lake front and western Jefferson Parish. (**B**) West bank communities opposite the City of New Orleans. (**C**) New Orleans East. (**D**) West bank communities on the opposite Mississippi River bank from Belle Chasse. The white lines are the HSDRRS floodwalls and levees enclosing GNO. The labeled white squares are the locations of the available continuous GPS stations. The underlying optical image is provided by Esri, HERE, OpenStreetMap.

from the river on the west bank (Fig. 5B), appear to be experiencing substantial elevation loss (−2 to <−20 mm/year). The areas of east bank Jefferson Parish west of the Lake Pontchartrain Causeway bridge display increasing elevation loss from east to west, with maximum rates of −27 mm/year measured at the recently expanded Louis Armstrong International Airport. Substantial elevation loss also occurs in New Orleans East (Fig. 5C) and in the west bank communities distal from the Mississippi River (Fig. 5D). We interpret these elevation loss trends as being caused by ground subsidence of multiple origins. Areas along Lake Pontchartrain from New Orleans East to the western edge the HSDRRS in Kenner distal from the Mississippi River are areas that were developed beginning in the mid-20th century and had been drained to convert low elevation swamp to build sites. This has resulted in elevations that are in places below mean sea level (Fig. 1C) due to a combination of compaction and oxidation of peaty soils subjected to phreatic conditions (*8*). Recent urbanization and expansion of residential communities have occurred along the west bank of the Mississippi River (Fig. 5D) in the past two decades. Jones *et al.* (*16*) attributed these areas of high ground elevation loss to subsidence due to settling of soils post-construction. We interpret a hot spot of elevation loss at rates of <−20 mm/year around New Orleans International Airport (Fig. 5A) as due to the soil disturbance associated with construction of a new terminal in 2016–2019.

The results show other circular areas of high elevation loss across GNO associated with industrial facilities (circled in Fig. 5). Jones *et al.* (*16*) identified several of these as industrial sites harvesting groundwater for cooling, resulting in a subsidence associated with groundwater cone of depression. High rates that we observed at other sites may be a byproduct of recent construction or deconstruction of decommissioned sites. A circular hot spot is also present west of the MARY GPS at the location of the Orleans Parish landfill (Fig. 5C).

The Michoud area, northeast of the city (Fig. 5C), shows apparent elevation increase. High rates of subsidence, interpreted as a consequence of groundwater extraction for cooling by an Entergy Inc., power plant at the site (Fig. 6) (*15*), affected this area until 2016 (Fig. 3A). After 2016, the closure of the power plant and the consequent cessation of groundwater pumping for coolant water in the area has apparently resulted in recovery of the water table levels and uplift at the surface at rates up to +6 mm/year. This pumping and recovery are occurring below an impermeable clay layer that confines the near surface aquifer (*1*, *35*). As mentioned before, we observed a second area of apparent elevation gain, with no clear causatory mechanism, near Belle Chasse, west of the river in the English Turn bend (e.g., near ENG5) (Fig. 5D). Last, scattered elevation gain is present in St. Bernard Parish along the Poydras to Reggio corridor in residential areas recently enclosed by the HSDRRS (Fig. 5D). In both areas, the measured ground motion could be a product of the land cover surrounding the residential areas, constituted by marshes and wetlands, which potentially dominate the detected InSAR signal, more than the one coming directly from the man-made structures.

Recent deformation in wetland areas

The S1A results in the present study, unlike in earlier InSAR studies and when using RSAT imagery, show measurable elevation change in some remnant wetland areas within and immediately outside the HSDRRS in New Orleans East, over the CWU located opposite the Violet Canal, and on the upriver portion of the west bank of the Mississippi River adjacent to the newly constructed HSDRRS in the

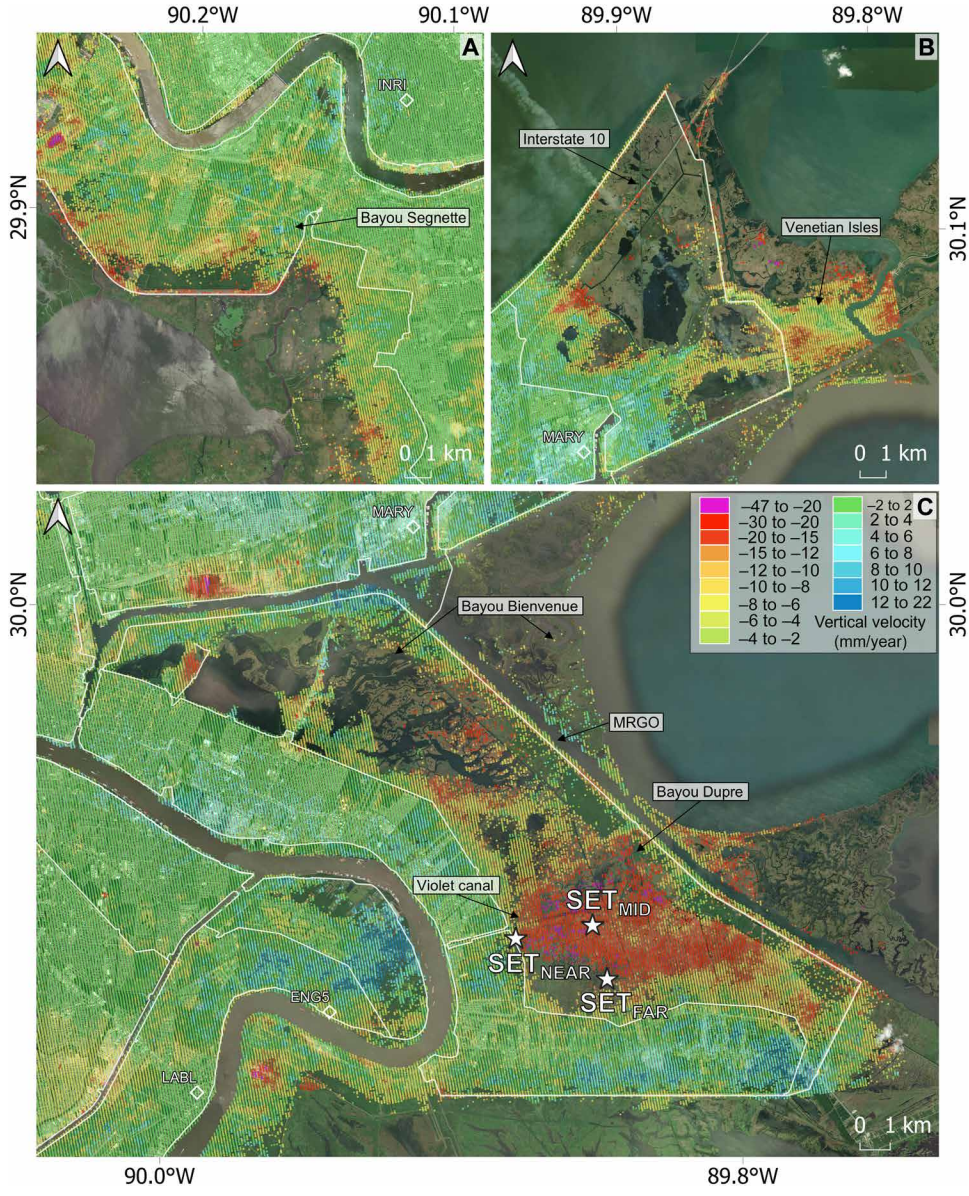

Fig. 6. Relative vertical velocity maps of the main wetland areas affected by substantial elevation change between 2016 and 2020. (**A**) Bayou Segnette region. (**B**) New Orleans East. (**C**) The Violet Canal area and adjacent parts of the Central Wetlands Unit. The white stars are the location of the surface-elevation table (SET) sites measured in (*43*) and referred to in Fig. 7. The white lines are the extent of the HSDRRS enclosing the city of New Orleans. The labeled white squares are the locations of the available continuous GPS stations. The underlying optical image is provided by Esri, HERE, OpenStreetMap.

Bayou Segnette region (Fig. 6). Rates of land elevation loss in these areas range from −2 to −37 mm/year and are generally higher than those observed in urbanized sections of GNO outside of hot spots around industrial facilities. Many of these were also encompassed by HSDRRS after the RSAT dataset was acquired (2005–2007) and, hence, are now experiencing restricted tidal exchange with adjacent wetlands and the Gulf.

In New Orleans East, a wetland area of high elevation loss (−6 to −30 mm/year; Fig. 6B) is present both inside and outside the HSDRRS. The results also show high elevation loss along Interstate-10 where it crosses the northern portion of the wetland. An exception to these high rates is the developed area around the community of Venetian Isles which lies outside the HSDRRS. Most of the detected surface motion falls outside the HSDRRS, suggesting that, in this case, the rapid elevation loss is not due to restricted tidal exchange and starvation of nutrients and mineral sediment resulting from their hydrological isolation. Further, coastal land loss maps for this region from 1932 to 2016 (*38*) show that much of the wetland loss is marsh edge retreat due to wave attack rather than internal ponding attributed to subsidence at rates that lead to marsh drowning (*39*). While the complex mechanisms operating to create subsidence in coastal wetlands of Louisiana remain poorly constrained, the most recent attempt to summarize the multiple mechanisms involved and to create a spatial map of rates, the 2023 Louisiana Coastal Master Plan (*40*),

reported elevation loss values between −2 and −6 mm/year for the New Orleans East area, far less than the ones observed in this study.

The maximum negative rates for wetland areas imaged by S1A (<−40 mm/year) are over the CWU opposite the Violet Canal and extending on both sides of the HSDRRS barrier (Fig. 6C). Keogh *et al.* (*32*) recognized that subsidence in MD wetlands is primarily focused within the first 1- to 3-m-thick organic-rich surficial layer where young, water-rich sediments were highly compressible. Hence, these areas might be expected to be experiencing more rapid elevation loss due to subsidence than urbanized portions of the GNO study area where the wetland layer is not present. However, it should be noted that inferring that these velocity rates are solely related to subsidence in wetland areas is complicated by natural deposition/erosion patterns. Jankowski *et al.* (*31*) used 274 RSET stations from across southern Louisiana wetlands to derive shallow [above the foundation rod of the surface-elevation table (SET)] subsidence rates (SS) from measured surface elevation change (SEC) and vertical accretion (VA) of organic and mineral matter at each station. For the 185 stations in the MD, they find means of SEC = +5.7 mm/year (range, −41 to +46 mm/year), VA = +12.8 mm/year (range, +1.6 to +83.7 mm/year), and SS = +7.1 mm/year (range, −39 to +60.7 mm/year). We can infer from these values that SEC and VA are highly site specific in MD wetlands. Five brackish and intermediate wetland sites in the SET network are located in the area of InSAR relative velocities shown in Fig. 6C, three in the Violet area and two in the areas immediately inside and outside HSDRRS in New Orleans East. While the dataset by Jankowski *et al.* (*31*) extends from station installation (earliest 2008) only to 2016 (updated data available from www.lacoast.gov/CRMS/), SEC measured at four of the five stations shows uplift (VA > SS) of +1.1 to +6.4 mm/year (one station in New Orleans East was −6.7 mm/year). Semiannual VA measurements were also relatively high over the period of record (range from +2.8 to +37.4 mm/year) for these stations. However, the reliability of the SET measurements is uncertain because the unsleeved and unanchored reference steel rods, despite being driven to refusal, potentially record the consolidation of the entire sediment sequence including tectonic processes (*41*). Given that it is unknown whether SET measures none, all, or part of the sediment sequence below its footing, this calls into question the quantitative comparison with InSAR. The InSAR-derived relative velocities, which are similar to the SET SEC measurement, show substantial elevation loss over the 2016–2020 interval, while the SET records do not. Further, InSAR rates are high enough that, given the low elevation of this wetland (the five SET stations are between 0.3- and 25.9-cm NAVD88, Geoid 12A), conversion to open water would be predicted within the next decade. In any case, the interpretation of the InSAR results obtained over vegetated and, in particular, wetlands areas must be done with caution considering the higher uncertainties levels and the high degree of complexity of such areas. An alternative explanation, at least for the CWU region, if not for the New Orleans East and wetland areas on the west bank of the Mississippi River Gulf Outlet Canal adjacent to the HSDRRS (Fig. 6C), relates to previous studies by Lane *et al.* (*42*) and Hunter *et al.* (*43*). They used RSETs driven ~4 m into the substrate to monitor elevation change in the late 1990s and again in 2011 after Hurricane Katrina affected the Central Wetlands/Violet area in 2005. The results by Hunter *et al.* (*43*) show rates of elevation change before Hurricane Katrina somewhat comparable to the 2016–2020 InSAR results (Fig. 7). Following Katrina, the 2011

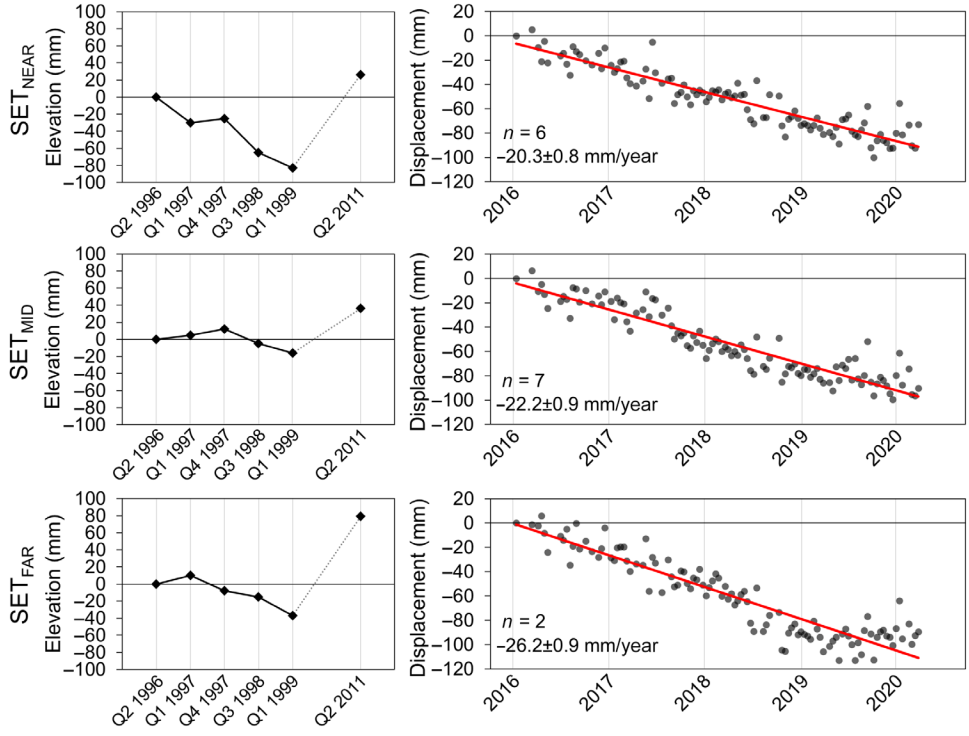

Fig. 7. Elevation change rates in CWU. Left: Elevation changes at the three SET stations measured by (*43*) between Q2 1996 and Q1 2011 in the Violet Canal area. Note the increased elevation in Q2 2011 due to the Katrina hurricane deposits. Right: Average displacement time-series (2016–2020) of all the InSAR points (*n*) in a 100 m radius around each SET station. The reported rates are the average rates for the entire period.

SET results show a rebound of surface elevation that they attribute to organic debris and sediment brought in by the storm. However, the later RSET sites have foundations that are driven 20 to 26 m into the substrate, and three of the five sites reached the Pleistocene (see the Supplementary Materials) (*31*). Because the SEC results from the deeper foundations of these later stations do not support the high relative elevation losses observed in the 2016–2020 S1A results, we are left to conclude that rapid subsidence in the Pleistocene (below the measurement interval of the SETs) is unlikely (*27*). However, our measured rates of elevation loss on the adjacent sections of the HSDRRS floodwalls (−10 to −20 mm/year) supports the high rates of elevation loss in the Bayou Dupre area (Fig. 6C), suggesting that both are responding to the same process and that surficial organic-rich soil compression (not present under the floodwalls) is not the cause. We cannot resolve this apparent contradiction (high versus low rates of elevation loss) with the present data. However, a contributing factor may be that most of the wetlands showing higher temporal coherence values (fig. S3) are in areas that, after construction of HSDRRS, have water level changes complicated by pumped removal of water causing shrink-swell of surficial sediments in addition to tidal exchange occurring when the gates in the floodwalls are open. Further, in the Violet Canal area, these privately owned marshlands are regularly subjected to controlled burning to regenerate food crops for waterfowl that are hunted on the property. Likely those burns, which potentially could cause ground surface deflation as the organic soil component is consumed, were not extended into the 1-km^2 exclusion areas for the state of Louisiana operated SET sites in the area (Fig. 6). We also did not observe high rates of displacement in the final year of the InSAR time series at the SET_{FAR} station between 2019 and 2020 (Fig. 7). Hence, anthropogenically affected inundation and marsh canopy heights may be a complicating factor in interpreting these InSAR results. Another point to consider when comparing the InSAR and the SET results is the different portion of wetland each of the two techniques measures. Our InSAR results have a pixel size of 60 m by 60 m, which averages the complex phase contribution of a much larger variety of wetland area. On the other end, the SET stations are point measurements centered over a centimetric area; hence, the rates are only very local.

Elevation loss of the HSDRRS since construction

The HSDRRS flood protection system installed around GNO post-Katrina and completed in 2012–2017 is an enclosing system of 350 miles (563 km) of levees and concrete floodwalls with 73 non-federal pumping stations, three canal closure structures with pumps, and four gated outlets to control tidal exchange and floodwater removal with the adjacent coastal system, lakes, and the Mississippi River. The structural elements of HSDRRS built by the US Army Corps of Engineers through 469 construction contract awards (from www.mvn.usace.army.mil/Missions/HSDRRS/) are at elevations designed to reduce the risk associated with a storm surge that has a 1% chance of occurring in any given year or a 100-year storm surge. Any relative elevation loss due to either loading induced deformation caused by the weight of the more recent structures or to deeper, regional subsidence of a geological or groundwater removal causality could degrade the level of storm protection offered by HSDRRS by decreasing wall/levee heights relative to sea level. This is in addition to any changes caused by sea level rise. InSAR time-series analysis can successfully monitor surface deformations affecting linear infrastructure networks and can be integrated with conventional ground-based monitoring systems for geotechnical applications (*44*). An early study (*45*) demonstrated the effectiveness of using displacement rates derived from the analysis of high-resolution X-band SAR data to evaluate and monitor the health of portions of levees in central New Orleans.

Here, we extracted the S1A-derived 2016–2020 vertical velocity rates from five sections of the HSDRRS spanning a total of 180 km. To isolate the deformations associated with HSDRRS elements, we obtained velocity rates by interpolating through an Inverse Distance Weighting method the InSAR points located in a 50-m buffer around the levee center line (provided by the National Levee Database, https://levees.sec.usace.army.mil) selected to have a sufficient number (at least 3) of InSAR points within the buffer to be used in the interpolation. We extracted the displacement rates corresponding to each pixel together with the corresponding height values along the levee center line and depicted as along-structure transects (segments A-to-H shown on Fig. 3) in Fig. 8. The highest rates of elevation loss (<−10 mm/year) are along the southern section of the A-to-B floodwalls constructed adjacent to New Orleans International Airport, in the central segment of earthen levees along B-to-D in New Orleans East, in the St. Bernard Parish floodwall section (east bank of Mississippi River) opposite the areas of high apparent elevation loss in adjacent wetlands discussed in the previous section (central E-to-F), and along the west bank of the Mississippi River on western segment G-to-H. In general, these are in areas of newly constructed concrete floodwall protection, as opposed to existing earthen levees like those along the Mississippi River and Lake Pontchartrain that were raised in some areas to meet HSDRRS standards. This suggests that post-construction settling of the floodwalls and their foundational underpinnings may be a primary mechanism for the observed areas of high velocity, with the exception of those areas adjacent to broader wetland areas of apparent high deformation discussed in the previous section. Diverse methods were used to construct the HSDRRS barrier including construction of new earthen levees, raising or armoring existing earthen levees, construction of concrete (T-wall) floodwalls, and modification of existing floodwalls by altering foundation depths or armoring. Foundation depths of newly constructed features were varied depending on local, near surface soil/geological character, and a variety of armoring of the outward face of the barriers were used including rip-rap, concrete revetment, and full versus toe armoring (see www.mvn.usace.army.mil/Missions/HSDRRS/ for details).

Following completion, HSDRRS was turned over for operation and maintenance to the state of Louisiana who manages it through parish-level levee boards with maintenance funding individualized by each of the four parishes (e.g., Orleans, Jefferson, St. Bernard, and Plaquemines) that sections pass through. This has meant that, since completion, monitoring of barrier elevation by real-time kinematic (RTK) GPS surveys has been incomplete and, in some cases, local efforts have been made to raise earthen sections by soil placement along short segments where elevation losses were identified by RTK GPS. The InSAR results in Fig. 8 are a compilation averaged over 60-m grid cells of the earthen or concrete barrier, the armored and unarmored sloping faces of the constructed element, and immediately adjacent areas of diverse substrate. These factors together make it difficult to ascribe exact causality (loading versus underlying subsidence) to the observed velocities in Fig. 8. They do indicate that certain segments of the barrier or elements of those segments (i.e., walls and reveted or rip-rapped slopes) are experiencing elevation

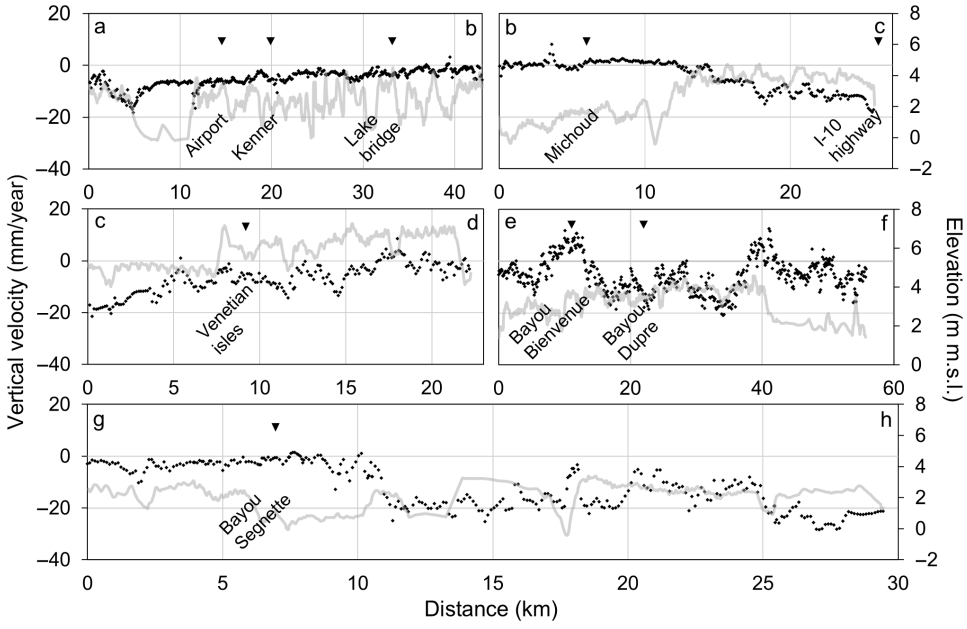

Fig. 8. Vertical velocity rates along the HSDRRS. Average vertical velocities (black dotted lines) and elevations (gray lines) in m above mean sea level (m.s.l.) extracted along sections of the HSDRRS flood protection system. The location of segments A to H is shown on Fig. 3B. The reported distance (in kilometers) is relative to the beginning of each section.

loss at rates up to an order of magnitude larger than those of absolute sea level rise of around +3.6 mm/year (*46*), reaching rates comparable to the 2050 projected rates for the Gulf Coast of up to +15 mm/year (*47*). Rising sea levels will increase not only the height of tides and storm surges, altering coastal flood patterns across the US, but also their frequency, with major (potentially destructive) high tide flooding events (about 1.20 m above mean higher high water) becoming four times more common, from 0.08 events/year in 2020 to 0.3 events/year by 2050 (*47*). If the detected elevation loss in GNO continues at current trends, then it could locally exacerbate the impact of accelerating sea level rise and, consequently, increase the magnitude and frequency of flooding during storms. This poses a long-term threat to the HSDRRS protection level, particularly for the lowest elevation levees/floodwalls and those experiencing the greatest local elevation loss due to subsidence. The local distribution of recent deposits could also considerably affect these trends, in particular where peat occurs close to the surface (Fig. 2A). In such locations, the peat deposits are vulnerable to compaction and oxidation when dried out by low groundwater table levels, leading to further elevation loss (*8*). Situated in a bowl-shaped area (Fig. 2B), New Orleans relies entirely on the operation of multiple pumping stations to discharge water into nearby lakes and waterways to maintain the correct groundwater level during both dry periods and storm events (*7*). If groundwater levels are depressed below peat boundaries, it could create vadose pore water conditions favorable for future peat oxidation. This could potentially reduce the effectiveness of the flood protection system and increase flood depths in the interior for sites overlying these deposits.

These considerations highlight the need for continuous monitoring activities to obtain a comprehensive overview of the dynamics affecting ground motion in natural environments and built areas. Our results demonstrate that S1A presents a rapid and relatively low-cost way of monitoring elevation change along the HSDRRS and other coastal protection structures in Louisiana and elsewhere. If used as an element of a monitoring plan that included regular ground surveys of the entire length of the flood protection system, then it would allow for rapid identification of elevation deficits below certified protection limits for maintenance to maintain HSDRRS's level of hurricane storm surge protection.

MATERIALS AND METHODS

In this study, we analyzed the RSAT images using the SqueeSAR (*48*) algorithm, derived from the PSI (*37*) methodology, while the S1A data using a processing technique derived from the Small Baseline Subset (SBAS) (*49*). SAR satellites acquire images with an inclined angle from the zenith referred to as the line of sight (LOS). This acquisition angle implies that the resulting SAR signal contains both the vertical and horizontal components of any ground elevation change between acquired images. The decomposition of the measured movements in the two components (horizontal and vertical) is only possible if both ascending and descending acquisition geometries are available over the same area. Unfortunately, only the S1A images acquired with ascending orbit are available for southeast Louisiana, hence deconvolving the horizontal movements from the desired vertical change is not directly possible using the available data. However, we assumed that the horizontal movements present in the reference system of the area are negligible in the framework of the study and converted the movements from LOS to vertical considering the incidence angle of each measured point. Even if this approach is consistent with previous studies to which the results are compared, it may introduce a bias in the estimated vertical rates given that the InSAR signal along the LOS could still detect horizontal components of motion related to faulting activity in the area.

With the anticipated launch of the NASA-ISRO SAR (NISAR) Mission in 2025, high-resolution (3 to 10 m depending on the acquisition mode) L-band SAR data in both ascending and descending orbits will be consistently acquired at 12-day intervals, enabling separation of vertical land motion from the east-west horizontal component with the necessary accuracy to potentially isolate local horizontal and vertical movements in GNO. The NISAR mission has substantial impact also for wetland monitoring due to its long wavelength (24 cm), which has been shown to be advantageous for preserving coherence and facilitating interferogram unwrapping in vegetated environments (*50*), potentially allowing a more robust estimation of trends of surface motions in such areas.

The result of an InSAR processing is a set of points representing, as explained more in detail below, either a single or multiple objects on the ground, and containing information about the mean velocity and displacement time series of those objects. The ground motion measured through InSAR data is always relative to a local reference point, which should be located in a stable area and should present high and stable phase reflectivity with time. For this reason, validation of the obtained InSAR-detected movements, even if not strictly necessary, is generally achieved by comparing results with data obtained through ground-based techniques (e.g., GPS and geodetic leveling). In the GNO area, eight Continuously Operating Reference Stations are available as part of the Nevada Geodetic Laboratory (NGL) GPS Network. Among these stations, only five have been operative for a period of more than 5 years and can be used to obtain site-specific and reliable information of ground motion for validation of InSAR results (table S1). Table 1 and table S2, respectively, give the key characteristics of the InSAR datasets used in current and previous studies.

RADARSAT-1 processing

In this study, we processed the RSAT images to replicate and/or improve the results that Dixon *et al.* (*15*) obtained almost two decades ago over the same area. We analyzed 52 RSAT images covering the period from 15 April 2002 to 24 February 2007 [versus 33 images between 14 April 2002 to 24 February 2005 of Dixon *et al.* (*15*)] (Table 1 and table S2) using SqueeSAR, an advanced processing method evolved from the PSI technique used in the original processing of the data. The PSI technique quantifies motion of targets on the surface using phase differences between sequential SAR scenes at full resolution (single look). Optimal targets correspond to point-wise solid objects that maintain high and consistent signal backscattering for long periods, such as buildings, rock outcrops, and infrastructure, called permanent scatterers (PSs). The SqueeSAR approach extracts information not only from PS but also from objects characterized by similar high temporal variability (high temporal decorrelation) and, hence, lower quality of the reflected signal (e.g., vegetated areas, debris areas, or uncultivated land) called distributed scatterers (DSs). The core of this approach consists of four main steps (*48*): (i) All pixels in the SAR scenes are analyzed using the DespecKS space adaptive filter to average the ones presenting homogeneous-phase behavior and categorize them as PS or DS. By definition, a pixel is defined as DS when it presents a number of statistically homogeneous "brothers" greater than 10. The adaptive filter also reduces the speckle noise of the DS without changing the intensity and amplitude values of the PS; (ii) the complex coherence matrix is calculated for every set of DS previously obtained; (iii) a phase triangulation algorithm is then applied to the coherence matrix of each DS before any phase unwrapping; and (iv) both PS and DS are analyzed together using the standard PSI processing chain.

We used all possible connections between the 52 RSAT scenes to generate the interferogram network (1326 interferograms in total) (Table 1). We removed the initial topographic phase residuals using the 1–arc-sec (~30 m–by–30 m resolution) Shuttle Radar Topography Mission (SRTM) digital elevation model (DEM) (*51*). We carried out phase unwrapping with a three-dimensional phase unwrapping algorithm (*52*) and calculated and removed the atmospheric phase screen contributions by using spatiotemporal filtering considering the different frequency characteristics that the atmospheric phase has in space and time domains. Last, we generated the LOS displacement time-series and average velocities (then projected to the vertical direction) at full resolution (~15 m in range by 6 m in azimuth) for all the points presenting temporal coherence (from 0 to 1) above 0.60, which we selected to both replicate the coverage obtained by Dixon *et al.* (*15*) and to obtain reliable information by minimizing the number of points affected by high uncertainties. The selected reference point is located in a stable area around 5 km northeast of New Orleans city center at 29.9817° latitude and −90.1185° longitude (Fig. 3).

S1A processing

In the present study, we analyzed 114 S1A images covering the period from 28 January 2016 to 31 March 2020 (Table 1) using the SBAS technique, a lower-resolution approach capable of extracting information from the DS by multilooking (i.e., increasing) the original pixel size of the image to increase the signal-to-noise ratio in low coherence areas. We used the InSAR Scientific Computing Environment (ISCE) (*53*) software (version 2.3.0) to generate the interferogram stack. For each image date, we created six nearest-neighbor interferograms (662 in total) within a maximum temporal baseline of 168 days and applied a multilook factor of 25 and 4, respectively, in range and azimuth directions, to obtain a ground pixel size of ~60 m by 60 m. Then, we carried out the time-series analysis with the Miami INsar Time-series software in Python (MintPy) (*54*). To invert the interferograms network to LOS displacement time series (subsequently projected to the vertical direction), we used the inverse of covariance in a weighted least square estimator (*55*). We removed the residual phase due to topography with the 1–arc-sec SRTM DEM and corrected tropospheric delays with the ERA-5 Global Atmospheric Model as implemented in the Python-based Atmospheric Phase Screen package (*56*). We then modified the connection network by manually removing seven images (table S3) presenting strong atmospheric residuals and hence larger uncertainties, leaving a total of 107 images and 585 interferograms. We unwrapped the phase with SNAPHU (*57*) and applied bridging and phase-closure corrections (*54*) to minimize unwrapping errors. Last, we calculated the relative LOS displacement rates and uncertainties with a linear best fit to the time series. We masked out from the final results the points showing temporal coherence of below 0.20. We selected this threshold to maximize data coverage even in the low coherence areas (i.e., wetlands and along the flood walls) while excluding points dominated by noise. The selected reference point is located at 29.8547° latitude and −89.9877° longitude, around 70 m southwest of the LABL GPS station (Fig. 1). In full-resolution InSAR approaches, the pixel-by-pixel phase difference between triplets of interferograms must be zero (phase closure). When multilooking is carried out to reduce noise and increase coherence,

it can introduce a different term in each interferogram, which determines a nonzero phase closure mainly in the short temporal baseline interferograms (i.e., 12 days for S1A). This can cause non-negligible biases and phase inconsistencies in the final estimated velocities, particularly in areas where the land cover is characterized by changes of soil moisture and water content in vegetation (*58*). Using medium length interferometric pairs and applying phase closure corrections helped to lessen the impact of multilooking on the data, especially in CWU and other wetland areas within GNO.

Supplementary Materials

This PDF file includes:

Figs. S1 to S4
Tables S1 to S3
References

REFERENCES AND NOTES

1. M. A. Allison, B. T. Yuill, T. Tornqvist, F. Amelung, T. Dixon, G. Erkens, R. Stuurman, C. Jones, G. Milne, M. Steckler, J. Syvitski, P. Teatini, Coastal subsidence: Global risks and mitigation. *EOS Trans. Am. Geophys. Union* **97**, 22–27 (2016).
2. J. M. Nigg, J. Barnshaw, M. R. Torres, Hurricane Katrina and the flooding of New Orleans: Emergent issues in sheltering and temporary housing. *Ann. Am. Acad. Pol. Soc. Sci.* **604**, 113–128 (2006).
3. G. Wöppelmann, M. Marcos, Vertical land motion as a key to understanding sea level change and variability. *Rev. Geophys.* **54**, 64–92 (2016).
4. M. Shirzaei, J. Freymueller, T. E. Törnqvist, D. L. Galloway, T. Dura, P. S. J. Minderhoud, Measuring, modelling and projecting coastal land subsidence. *Nat. Rev. Earth Environ.* **2**, 40–58 (2021).
5. B. C. Frederick, M. Blum, R. Fillon, H. H. Roberts, Resolving the contributing factors to Mississippi Delta subsidence: Past and present. *Basin Res.* **31**, 171–190 (2019).
6. S. Yang, F. T.-C. Tsai, Understanding impacts of groundwater dynamics on flooding and levees in greater New Orleans. *J. Hydrol. Reg. Stud.* **32**, 100740 (2020).
7. L. Nougues, "Groundwater drainage in New Orleans" (Deltares Internship Report, TU Delft Civil Engineering and Geosciences, 2021); http://resolver.tudelft.nl/uuid:11aed00c-4de7-4626-820a-8c0f84e33b49.
8. S. van Asselen, G. Erkens, M. E. Keogh, R. Stuurman, Shallow-subsidence vulnerability in the city of New Orleans, Southern USA. *Hydrgeol. J.* **32**, 867–889 (2024).
9. M. Schleistein, "Mississippi River will rise to top of lowest New Orleans levees as possible hurricane nears, experts say" (2019); www.nola.com.
10. S. Dangendorf, N. Hendricks, Q. Sun, J. Klinck, T. Ezer, T. Frederikse, F. Calafat, T. Wahl, T. Törnqvist, Acceleration of U.S. Southeast and Gulf coast sea-level rise amplified by internal climate variability. *Nat. Commun.* **14**, 1935 (2023).
11. City of New Orleans, "Extent depth of flooding Katrina" (2005); https://nola.gov/nola/media/Safety-and-Permits/floodplain-management/Extent-Depth-of-Flooding-Katrina.pdf.
12. B. Osmanoğlu, F. Sunar, S. Wdowinski, E. Cabral-Cano, Time series analysis of InSAR data: Methods and trends. *ISPRS J. Photogramm. Remote Sens.* **115**, 90–102 (2016).
13. E. Chaussard, F. Amelung, H. Abidin, S.-H. Hong, Sinking cities in Indonesia: ALOS PALSAR detects rapid subsidence due to groundwater and gas extraction. *Remote Sens. Environ.* **128**, 150–161 (2013).
14. F. E. Dunn, P. S. J. Minderhoud, Sedimentation strategies provide effective but limited mitigation of relative sea-level rise in the Mekong delta. *Commun. Earth Environ.* **3**, 2 (2022).
15. T. H. Dixon, F. Amelung, A. Ferretti, F. Novali, F. Rocca, R. Dokka, G. Sella, S. W. Kim, S. Wdowinski, D. Whitman, Space geodesy: Subsidence and flooding in New Orleans. *Nature* **441**, 587–588 (2006).
16. C. E. Jones, K. An, R. G. Blom, J. D. Kent, E. R. Ivins, D. Bekaert, Anthropogenic and geologic influences on subsidence in the vicinity of New Orleans, Louisiana. *J. Geophys. Res. Solid Earth* **121**, 3867–3887 (2016).
17. US Army Corps of Engineers (2019); www.mvn.usace.army.mil/Media/News-Releases/Article/2035709/hsdrrs-levee-lift-draft-general-re-evaluation-reports-available-for-review/.
18. T. A. Meckel, An attempt to reconcile subsidence rates determined from various techniques in southern Louisiana. *Quat. Sci. Rev.* **27**, 1517–1522 (2008).
19. T. E. Törnqvist, S. J. Bick, K. van der Borg, A. F. M. de Jong, How stable is the Mississippi Delta? *Geology* **34**, 697–700 (2006).
20. R. K. Dokka, G. F. Sella, T. H. Dixon, Tectonic control of subsidence and southward displacement of southeast Louisiana with respect to stable North America. *Geophys. Res. Lett.* **33**, L23308 (2006).
21. R. K. Dokka, The role of deep processes in late 20th century subsidence of New Orleans and coastal areas of southern Louisiana and Mississippi. *J. Geophys. Res.* **116**, B06403 (2011).
22. M. A. Karegar, T. H. Dixon, R. Malservisi, A three-dimensional surface velocity field for the Mississippi Delta: Implications for coast-al restoration and flood potential. *Geology* **43**, 519–522 (2015).
23. M. A. Karegar, K. M. Larson, J. Kusche, T. H. Dixon, Novel quantification of shallow sediment compaction by GPS interferometric reflectometry and implications for flood susceptibility. *Geophys. Res. Lett.* **47**, e2020GL087807 (2020).
24. K. Shinkle, R. K. Dokka, "Rates of vertical displacement at benchmarks in the Lower Mississippi Valley and the Northern Gulf Coast" (NOAA Tech. Rep. no. 50, 2004), pp. 1–135.
25. A. S. Kolker, M. A. Allison, S. Hameed, An evaluation of subsidence rates and sea-level variability in the Northern Gulf of Mexico. *Geophys. Res. Lett.* **38**, 21404 (2011).
26. G. Z. Voyiadjis, Y. Zhou, Time-dependent modeling of subsidence due to drainage in bounding shales: Application to a depleted gas field in Louisiana. *J. Petrol. Sci. Eng.* **166**, 175–187 (2018).
27. M. E. Keogh, T. E. Törnqvist, Measuring rates of present-day relative sea-level rise in low-elevation coastal zones: A critical evaluation. *Ocean Sci.* **15**, 61–73 (2019).
28. R. J. Edwards, Mid-to late-Holocene relative sea-level change in southwest Britain and the influence of sediment compaction. *Holocene* **16**, 575–587 (2006).
29. S. Mazzotti, A. Lambert, M. Van der Kooij, A. Mainville, Impact of anthropogenic subsidence on relative sea-level rise in the Fraser River delta. *Geology* **37**, 771–774 (2009).
30. B. P. Horton, S. E. Engelhart, D. F. Hill, A. C. Kemp, D. Nikitina, K. G. Miller, W. R. Peltier, Influence of tidal-range change and sediment compaction on Holocene relative sea-level change in New Jersey, USA. *J. Quaternary Sci.* **28**, 403–411 (2013).
31. K. L. Jankowski, T. E. Törnqvist, A. M. Fernandes, Vulnerability of Louisiana's coastal wetlands to present-day rates of relative sea-level rise. *Nat. Commun.* **8**, 14792 (2017).
32. M. E. Keogh, T. E. Tornqvist, A. S. Kolker, G. Erkens, J. G. Bridgeman, Organic matter accretion, shallow subsidence, and river delta sustainability. *J. Geophys. Res. Earth Surf.* **126**, e2021JF006231 (2021).
33. B. Yuill, D. Lavoie, D. J. Reed, Understanding subsidence processes in coastal Louisiana. *J. Coast. Res.* **10054**, 23–36 (2009).
34. F. Qu, Z. Lu, J. O. Kim, M. J. Turco, Mapping and characterizing land deformation during 2007–2011 over the Gulf Coast by L-band InSAR. *Remote Sens. Environ.* **284**, 113342 (2023).
35. L. O. Ohenhen, M. Shirzaei, C. Ojha, S. F. Sherpa, R. J. Nicholls, Disappearing cities on US coasts. *Nature* **627**, 108–115 (2024).
36. K. Wang, J. Chen, E. Valseth, G. Wells, S. Bettadpur, C. E. Jones, C. Dawson, Subtle land subsidence elevates future storm surge risks along the Gulf Coast of the United States. *J. Geophys. Res. Earth* **129**, e2024JF007858 (2024).
37. A. Ferretti, C. Prati, F. Rocca, Permanent scatterers in SAR interferometry. *IEEE Trans. Geosci. Remote Sens.* **39**, 8–20 (2001).
38. B. R. Couvillion, H. Beck, D. Schoolmaster, M. Fischer, "Land Area Change in Coastal Louisiana (1932 to 2016)" (2017); https://pubs.usgs.gov/sim/3381/sim3381.pdf.
39. R. D. Delaune, J. A. Nyman, W. H. Patrick, Peat collapse, ponding and wetland loss in a rapidly submerging coastal marsh. *J. Coast. Res.* **10**, 1021–1030 (1994).
40. C. Fitzpatrick, K. L. Jankowski, D. Reed, D, "2023 Coastal Master Plan: Attachment B3: Determining Subsidence Rates for Use in Predictive Modeling. Version 3. (p. 71). Baton Rouge, Louisiana: Coastal Protection and Restoration Authority" (2021); https://coastal.la.gov/wp-content/uploads/2023/08/B3_DeterminingSubsidenceRates_Mar2021_v3.pdf.
41. M. R. Byrnes, J. L. Berlinghoff, R. J. Hollis, R. Johnson, T. Miller, "Stability of Reference Monuments for Documenting Elevation Changes in Consolidating Holocene Sediment in South Louisiana Coastal Environments. Final Report prepared for Coastal Protection and Restoration Authority of Louisiana, Baton Rouge, LA, 17 p. plus Appendices" (2023); https://cims.coastal.la.gov/DocLibrary/FileDownload.aspx?Root=0&id=28018.
42. R. R. Lane, J. W. Day, J. N. Day, Wetland surface elevation, vertical accretion, and subsidence at three Louisiana Estuaries receiving diverted Mississippi River water. *Wetlands* **26**, 1130–1142 (2006).
43. R. G. Hunter, J. W. Day, G. P. Shaffer, R. R. Lane, A. J. Englande, R. Reimers, D. Kandalepas, W. B. Wood, J. N. Day, E. Hillmann, Restoration and management of a degraded Baldcypress swamp and freshwater marsh in Coastal Louisiana. *Water* **8**, 71 (2016).
44. V. Macchiarulo, P. Milillo, C. Blenkinsopp, G. Giardina, Monitoring deformations of infrastructure networks: A fully automated GIS integration and analysis of InSAR time-series. *Struct. Health Monit.* **21**, 1849–1878 (2022).
45. D. D. C. Nguyen, V. Bennett, K. O'Meara, New Orleans levee displacement study via interferometric point target analysis technique and in situ instrumentation. *J. Geotech. Geoenviron. Eng.* **14**, 8 (2019).
46. R. Lindsey, "Climate change: Global sea level" (2023); www.climate.gov/news-features/understanding-climate/climate-change-global-sea-level.
47. W. V. Sweet, B. D. Hamlington, R. E. Kopp, C. P. Weaver, P. L. Barnard, D. Bekaert, W. Brooks, M. Craghan, G. Dusek, T. Frederikse, G. Garner, A. S. Genz, J. P. Krasting, E. Larour, D. Marcy, J. J. Marra, J. Obeysekera, M. Osler, M. Pendleton, D. Roman, L. Schmied, W. Veatch,

K. D. White, C. Zuzak, "Global and Regional Sea Level Rise Scenarios for the United States: Updated Mean Projections and Extreme Water Level Probabilities Along U.S. Coastlines" (NOAA Tech. Rep. NOS 01, National Oceanic and Atmospheric Administration, National Ocean Service, 2022); https://earth.gov/sealevel/us/internal_resources/756/noaa-nos-techrpt01-global-regional-SLR-scenarios-US.pdf.
48. A. Ferretti, A. Fumagalli, F. Novali, C. Prati, F. Rocca, A. Rucci, A new algorithm for processing interferometric data-stacks: SqueeSAR. *IEEE Geosci. Remote Sens. Lett.* **49**, 3460–3470 (2011).
49. P. Berardino, G. Fornaro, R. Lanari, E. Sansosti, A new algorithm for surface deformation monitoring based on small baseline differential SAR interferograms. *IEEE Trans. Geosci. Remote Sens.* **40**, 2375–2383 (2002).
50. S. Wdowinski, S-H. Hong, "Wetland InSAR: A review of the technique and applications" in *Remote Sensing of Wetlands*. R. Tiner, M. Laneg, V. Klemas, Eds. (CRC Press, 2015) pp. 154–171.
51. T. G. Farr, P. A. Rosen, E. Caro, R. Crippen, R. Duren, S. Hensley, M. Kobrick, M. Paller, E. Rodriguez, L. Roth, D. Seal, S. Shaffer, J. Shimada, J. Umland, M. Werner, M. Oskin, D. Burbank, D. Alsdorf, The shuttle radar topography mission. *Rev. Geophys.* **45**, RG2004 (2007).
52. A. Hooper, H. A. Zebker, Phase unwrapping in three dimensions with application to InSAR time series. *J. Opt. Soc. Am. A* **24**, 2737–2747 (2007).
53. P. A. Rosen, E. Gurrola, G. F. Sacco, H. Zebker, "The InSAR scientific computing environment," in *Proceedings of the 9th European Conference on Synthetic Aperture Radar* (IEEE, 2012), pp. 730–733.
54. Y. Zhang, H. Fattahi, F. Amelung, Small baseline InSAR time series analysis: Unwrapping error correction and noise reduction. *Comput. Geosci.* **133**, 104331 (2019).
55. A. M. Guarnieri, S. Tebaldini, On the exploitation of target statistics for SAR interferometry applications. *IEEE Trans. Geosci. Remote Sens.* **46**, 3436–3443 (2008).
56. R. Jolivet, P. S. Agram, N. Y. Lin, M. Simons, M. P. Doin, G. Peltzer, Z. Li, Improving InSAR geodesy using global atmospheric models. *J. Geophys. Res. Solid Earth* **119**, 2324–2341 (2014).
57. C. W. Chen, H. A. Zebker, Two-dimensional phase unwrapping with use of statistical models for cost functions in nonlinear optimization. *J. Opt. Soc. Amer. A Opt. Image Sci. Vis.* **18**, 338–351 (2001).
58. Y. Maghsoudi, A. J. Hooper, T. J. Wright, M. Lazecky, H. Ansari, Characterizing and correcting phase biases in short-term multilooked interferograms. *Remote Sens. Environ.* **275**, 113022 (2022).
59. A. Nelson, "Hurricane Katrina - What Happened? A Field Trip. The Geology of the Katrina Disaster in New Orleans" (2015); www2.tulane.edu/~sanelson/Katrina/Hurricane%20Katrina%20Field%20Trip.pdf.
60. J. B. Dunbar, L. D. Britsch III, Geology of the New Orleans area and the canal levee failures. *J. Geotech. Geoenviron. Eng.* **134**, 566–582 (2008).
61. J. D. Rogers, G. P. Boutwell, D. W. Schmitz, D. Karadeniz, C. M. Watkins, A. Athanasopoulos-Zekkos, D. Cobos-Roa, Geologic conditions underlying the 2005 17th Street canal levee failure in New Orleans. *J. Geotech. Geoenviron. Eng.* **134**, 583–601 (2008).
62. A. Pepe, R. Lanari, On the extension of the minimum cost flow algorithm for phase unwrapping of multitemporal differential SAR interferograms. *IEEE Trans. Geosci. Remote Sens.* **44**, 2374–2383 (2006).
63. H. Fattahi, F. Amelung, InSAR bias and uncertainty due to the systematic and stochastic tropospheric delay. *J. Geophys. Res. Solid Earth* **120**, 8758–8773 (2015).

Acknowledgments: We thank our Louisiana Coastal Protection and Restoration Authority (CPRA) collaborators and project managers for support and valuable discussions of the results including J. Pahl, K. Jankowski, S. Khalil, A. Freeman, M. Green, A. Grace, and E. White. Additional assistance, with our thanks, to T. Tornqvist, R. Escobedo, B. Varugu, and A. Ferretti. We would like to also thank the anonymous reviewers for insightful comments. **Funding:** The CPRA provided funding for this project under the auspices of the Lower Mississippi River Management Program funded through the Gulf Research Program. C.E.J. was supported by the Jet Propulsion Laboratory, California Institute of Technology, under task order 80NM0018F059, contract 209249.04.02.01.13. **Authors contribution:** Writing—original draft: S.F., M.A.A., and C.E.J. Conceptualization: S.F., M.A.A., and C.E.J. Investigation: C.E.J. Writing—review and editing: S.F., M.A.A., and C.E.J. Methodology: S.F., M.A.A., and C.E.J. Resources: M.A.A. Data curation: S.F. and M.A. Validation: S.F. and C.E.J. Funding acquisition: M.A.A. Supervision: S.F., M.A., and C.E.J. Formal analysis: S.F. Project administration: M.A.A. Software: S.F. Visualization: S.F. and M.A.A. **Competing interests:** The authors declare that they have no competing interests. **Data and materials availability:** The InSAR vertical velocity rates produced in this work are available at https://doi.org/10.5281/zenodo.14984961. Raw RADARSAT-1 SAR images are provided by TRE-ALTAMIRA; level 1 SLC S1A SAR images are distributed by the Alaska Satellite Facility (ASF) Distributed Active Archive Center at https://search.asf.alaska.edu/; the US Geological Survey (USGS) $^{1}/_{3}$–arc-sec DEM is available from the USGS Science Data Catalog at https://data.usgs.gov/datacatalog/data/USGS:3a81321b-c153-416f-98b7-cc8e5f0e17c3. ISCE software is freely available at https://github.com/isce-framework/isce2 and https://zenodo.org/records/6961793; MintPy software is freely available at https://github.com/insarlab/MintPy and https://zenodo.org/records/13141904; GPS data are available from the NGL at https://geodesy.unr.edu/NGLStationPages/gpsnetmap/GPSNetMap.html. All other data needed to evaluate the conclusions in the paper are present in the paper and/or the Supplementary Material.

Submitted 28 September 2024
Accepted 21 May 2025
Published 27 June 2025
10.1126/sciadv.adt5046